Research Article | Vol. 31, No. 23 / 6 Nov 2023 / Optics Express 38744
Optics EXPRESS

High-sensitivity self-powered photodetector based on an in-situ prepared $CsPbBr_3$ microwire/InGaN heterojunction

LINGLING SUN,[1] JITAO LI,[1,2] JIAJIA HAN,[1] MING MENG,[1] BINGHUI LI,[3,5] AND MINGMING JIANG[4,*]

[1]School of Physics and Telecommunications Engineering, Zhoukou Normal University, Zhoukou 466001, China
[2]The Key Laboratory of Rare Earth Functional Materials of Henan Province, Zhoukou Normal University, Zhoukou 466001, China
[3]State Key Laboratory of Luminescence and Applications, Changchun Institute of Optics Fine Mechanics and Physics, Chinese Academy of Sciences, Changchun 130033, China
[4]College of Physics, MIIT Key Laboratory of Aerospace Information Materials and Physics, Key Laboratory for Intelligent Nano Materials and Devices, Nanjing University of Aeronautics and Astronautics, No. 29 Jiangjun Road, Nanjing 211106, China
[5]binghuili@163.com
*mmjiang@nuaa.edu.cn

Abstract: Low-dimensional $CsPbBr_3$ perovskite materials have gained widespread attention, derived from their remarkable properties and potential for numerous optoelectronic applications. Herein, the sample of $CsPbBr_3$ microwires were prepared horizontally onto n-type InGaN film substrate using an in-plane solution growth method. The resulting $CsPbBr_3$ microwire/InGaN heterojunction allows for the achievement of a highly sensitive and broadband photodetector. Particularly for the implementation in a self-supplying manner, the best-performing photodetector can achieve a superior On/Off ratio of 4.6×10^5, the largest responsivity ~ 800.0 mA/W, a maximum detectivity surpassing 4.6×10^{12} Jones, and a high external quantum efficiency approaching 86.5% upon 405 nm light illumination. A rapid response time (~ 4.48 ms/7.68 ms) was also achieved. The as-designed $CsPbBr_3$ microwire/InGaN heterojunction device without any encapsulation exhibits superior comprehensive stability. Besides, the device featuring as a single pixel imaging unit can readily detect simple images under broadband light illumination with a high spatial resolution, acknowledging its outstanding imaging capability. The robust photodetection properties could be derived from the intense absorption of $CsPbBr_3$ MWs and high-efficiency charge carriers transporting toward the in-situ formed $CsPbBr_3$/InGaN heterointerface. The results may offer an available strategy for the in-situ construction of best-performing low-dimensional perovskite heterojunction optoelectronic devices.

1. Introduction

The perovskite semiconductor, such as all-inorganic cesium lead halides, has gained widespread attentions, which were originally resulted from their distinguished properties like large absorption coefficient, wide spectral absorption range, well-controlled bandgap energies, high efficiency of light-to-electricity conversion, large value of carrier diffusion length, outstanding stability, etc [1–7]. They have been extensively used in solar cells, electroluminescent devices, photosensing devices, transistors and so on [8–15]. Currently, it is still facing the toughest challenge to prepare perovskite polycrystalline films with excellent quality, large-scale and high production, which greatly limited their realistic applications [16–20]. Compared with perovskite planar films, the product of single-crystalline perovskite with shape-controllable structures at micro and nanometer scale, possesses much more fantastic characteristics including well-defined

#505800 https://doi.org/10.1364/OE.505800
Journal © 2023 Received 13 Sep 2023; revised 10 Oct 2023; accepted 23 Oct 2023; published 31 Oct 2023

Optics EXPRESS

boundaries, sharp edges, atomically-smooth side facets and highly-crystallized quality, especially for their higher stability, charge transporting performances and low trap-state density [21–25]. By virtue of those properties, the wire-like structure perovskite monocrystals featuring as appealing optoelectronic materials enable them to meet realistic application demands, particularly for the achievement of photodetection devices with low energy consumption, miniaturization, wireless performance, independence, sustainability and ease of integration [26–35]. Due to the absence of single-crystalline perovskite planar films with large-scale fabrication, mature technology and industrialized manufacturing process, the realization of low-dimensional perovskite monocrystals self-biased photodetectors that meeting high sensitivity, low-power dissipation, high response speed and long-term stability, is still limited. It is desirable to design a rational device architecture to conquer the current drawbacks [36–39].

Considering the strong optical absorption characteristics of the low-dimensional perovskite monocrystals, constructing hybrid heterojunctions by combining inorganic semiconductors such as GaN, SiC, Si, ZnO and SnO_2, might be able to provide an alternative strategy to overcome the drawbacks mentioned above and achieve high-performance photodetectors [40–46]. By assembling low-dimensional perovskite crystals as light-harvesting materials, the construction of photodetection devices based on the above inorganic materials has been successfully realized, and demonstrated their potential in the applications. And most of those previously reported devices also exhibited several remarkable advantages of small size, low weight, and easy integration. Additionally, the mentioned inorganic materials could give rise to numerous benefits, such as the spectral broadening of photoresponse band, available passivation of trapping centers on its external facets and grain boundaries, thus enhancing the performances of photodetection devices [47–54]. Despite the significant progress made in the construction of low-dimensional perovskite monocrystals hybrid heterojunction photodetectors, the photoresponse properties are still suffered from the interfacial shortcomings, containing the lattice mismatch, leakage current, insufficient charge carriers transport between perovskite and inorganic semiconductor, interface trapping centers, nonrecombination loss, especially for the majority carrier transport and charge management capacities. Therefore, studies on the fabrication of single-crystalline perovskite heterostructure optoelectronic devices is still in the initial stage [7,55–58].

Comparatively, the InGaN planar material presents the characteristics of tunable bandgaps, outstanding electrical properties, mature doping processing and manufacturing technology, which makes it an ideal candidate to developing single-crystalline perovskite heterojunction optoelectronic devices [59–61]. Herein, we proposed and illustrated a facile scheme to prepare low-dimensional perovskite heterojunction, which was conducted by directly preparing $CsPbBr_3$ MWs produced from liquid precursors on n-type InGaN planar substrate. Photoelectrical measurements revealed that in-situ constructed $CsPbBr_3$ MW/InGaN heterostructure showed a remarkable rectifying characteristic and a pronounced photovoltaic behavior, illustrating its potential application of broadband photodetection capability. The device can also detect ultraviolet-visible lights in a self-driven mode, with photoresponse performances including the largest responsivity ~ 800.0 mA/W, a high specific detectivity of 4.6×10^{12} Jones, a high external quantum efficiency approaching 86.5%, a ultrafast responding time of 4.48/7.68 ms, and high light-to-dark current ratio of 4.6×10^4 when exposed to a 405 nm light irradiation. The device displayed a reliable stability and high-resolution imaging capability. Combined with the superior photoresponse, the in-situ fabricated $CsPbBr_3$/InGaN heterojunction could find potential to construct fast-speed, broadband and high-sensitivity photodetectors.

2. Experimental section

2.1. Samples preparation

The product of individual $CsPbBr_3$ MWs with centimete length and large-scale vertical monocrystalline structures was successfully prepared using an in-plane solution growth method [28,35,62].

Optics EXPRESS

The synthesizing process is briefly described as follows. (1) A mixture of CsBr and $PbBr_2$ with equal mole (~ 0.5 mM) was prepared in 1 mL dimethyl sulfoxide (DMSO). (2) The heating temperature of processed DMSO solution was raised up to 85 °C using a magnetic stirring heater, and then maintained at this temperature for about 10 h while stirring. (3) Afterwards, the solution cooled naturally to ambient temperature. (4) The resultant solution with 15 μL was then dripped on a 1.5×2.5 cm InGaN planar substrate (commercially-procured product, n-type conduction), and another InGaN film substrate with identical size was mechanically placed on the solution pre-covered substrate. (5) Keeping the sample for two days at ambient temperature, the upper InGaN film was taken away. The product of $CsPbBr_3$ wires was dispersed on the substrate individually, which were visible to the naked eye. The cross-sectional width of our synthesized samples ranges from hundreds nanometers, a few microns to dozens of micron levels. Besides, an individual $CsPbBr_3$ could be targeted on the InGaN substrate, and also could be mechanically transferred anywhere there is a need.

2.2. Devices fabrication

The device fabrication is outlined simply as follows [40,60,63]. (1) A single $CsPbBr_3$ MW was firstly calibrated on the InGaN substrate. (2) After removed the undesired $CsPbBr_3$ MWs, Ti/Al (55/35 nm) nanofilm was deposited on the n-InGaN film substrate via an electron-beam evaporation equipment. An annealing treatment at appropriate temperature in air atmosphere enabled the evaporated metal film forming good ohmic contact with n-type InGaN film substrate. (3) Using a mask plate, two 4 μm-MgO films were evaporated at the bilateral sides of the pre-calibrated $CsPbBr_3$ MW on the blank-InGaN film substrate utilizing an electron-beam evaporation. (4) Using spin-coated technology, a layer of poly (3,4-ethylenedioxythiophene):poly(styrene sulfonate) (PEDOT:PSS) polymer was prepared on a piece of ITO conducting glass, thus forming the PEDOT:PSS/ITO top transparent electrode. (5) Finally, the processed ITO/PEDOT:PSS film was reversely put on the $CsPbBr_3$ MW in the as-fabricated $CsPbBr_3$ MW/InGaN heterostructure. Thereby, the pre-prepared MgO films could block the direct touching between the ITO electrode and the underlying n-InGaN layer. A photodiode based on the as-proposed ITO/p-PEDOT:PSS/$CsPbBr_3$ MW/n-InGaN heterostructure photodiode is constructed. In the device, the Ti/Al (n-contact) and ITO/PEDOT:PSS (p-contact) featured as metal electrodes for the photocarrier collection.

2.3. Characterization and analysis

Surface outlines and element constituents of as-synthesized products were tested utilizing a scanning electron microscope (SEM, Hitachi), which was embedded with energy disperse spectroscopy (EDS) mapping. Powder X-ray diffraction (XRD) was conducted to check the crystalline structures of $CsPbBr_3$ samples. X-ray photoelectron spectrometer (XPS) was utilized to investigate the elemental compositions and valence states of the samples. Ultraviolet-visible spectrophotometer (UV-Vis, Shimadzu) were used to determine the absorbance spectra and diffuse reflectance spectra. The electrical performances via current(I)–voltage(V) of $CsPbBr_3$ MWs, n-InGaN layer and the resulting $CsPbBr_3$/InGaN heterostructure devices were measured using a Keysight B1500A. While their photoresponse and photoelectric properties were evaluated using a testing system, which included a Keysight B1500A, monochromator and EQ-99 laser light source. A nanosecond laser combined with a Tektronix signal oscilloscope was utilized to detect the transient results.

3. Results and discussions

As we described in Experimental Section, the product of individual $CsPbBr_3$ MWs having monocrystalline properties and centimeters in length were prepared. Figure 1(a) images a typical SEM photograph of a monocrystalline $CsPbBr_3$ wirelike structure, showing a shape of typical

Optics EXPRESS

microribbon with smooth side facets, uniform and straight edges. The cross-section width is approximately 30 μm. The chemical composition and elemental distribution of a $CsPbBr_3$ wire was examined, and the EDS elemental mapping images are shown in Fig. 1(a). Obviously, three species of Cs, Pb and Br are homogeneously distributed within the MW. The XRD spectrum of $CsPbBr_3$ monocrystalline samples is demonstrated in Fig. 1(b). Two sharp diffraction peaking at 15.3° and 30.8° are identified as the crystallographic planes of (100) and (200) of standard orthorhombic $CsPbBr_3$ crystals, respectively [22,26,32]. Optical characterization of a $CsPbBr_3$ monocrystalline MW was performed. Being excited optically utilizing a 405 nm laser source, the photoluminescence (PL) spectrum in Fig. 1(c) (Left) illustrates that the sample emits at a predominant wavelength of 530.5 nm with a bandwidth of about 26.5 nm; while the absorption line is exhibited in Fig. 1(c) (Right). Besides, the absorption of as-synthesized $CsPbBr_3$ monocrystalline MWs is sharply edged at 546.25 nm, which manifests that the optical bandgap is calculated to about 2.27 eV (Inset in Fig. 1(c)). These outcomes indicate that the sample of $CsPbBr_3$ monocrystalline wires was productively prepared using a low-budget, operation-friendly, solution-processed scheme [28–30].

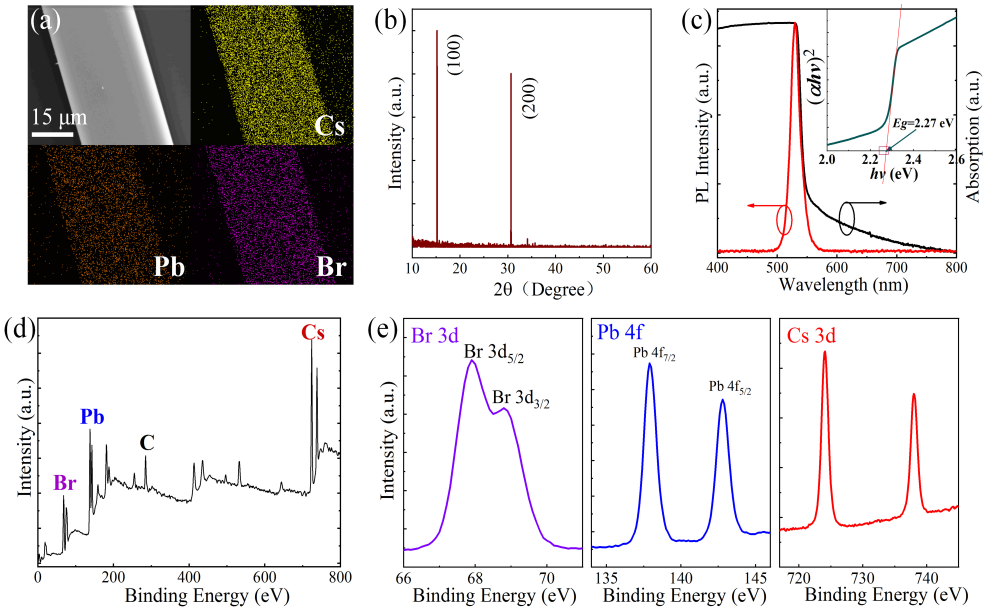

Fig. 1. Characterization of as-prepared $CsPbBr_3$ microcrystals. (a) SEM photograph of a $CsPbBr_3$ wire and its EDS mapping of element composition. (b) XRD identification of as-synthesized $CsPbBr_3$ wires. (c) The resulting absorption (Right) and PL (Left) spectra of a $CsPbBr_3$ MW. Inset: the plotted $(\alpha h\nu)^2 - h\nu$ curve indicates the fitted optical bandgap of $CsPbBr_3$ microcrystals ~ 2.27 eV. (d) XPS analysis of the $CsPbBr_3$ MWs. (e) High-definition XPS spectra for Br 3d, Pb 4f and Cs 3d, respectively.

The monocrystalline structures of as-prepared $CsPbBr_3$ products were examined using XPS measurement, which determines the presence of Cs, Pb and Br species. Figure 1(d) reveals XPS analysis of as-grown $CsPbBr_3$ monocrystalline wires. The resulting high-definition views of Br 3d, Pb 4f, and Cs 3d are further illustrated in Fig. 1(e), which are conducted to exhibit their electronic states in more detail. The Br 3d spectrum, which contains a strong $3d_{3/2}$ and much weaker $3d_{5/2}$ subpeaks, are distinctly observed (the left). In this case, the Br 3d spectrum confirms the existence of Br^- cations. Second, the Pb 4f spectrum, which is composed of $4f_{5/2}$ and $4f_{7/2}$ centering at 142.93 and 138.25 eV, respectively, is corresponding to Pb^{2+} cations.

Optics EXPRESS

Third, the presence of Cs^+ cations is confirmed owing to the observation of the Cs $3d_{5/2}$ and $3d_{3/2}$, which are centering at 724.3 eV and 738.2 eV, respectively. The XPS analysis suggests that individual $CsPbBr_3$ monocrystalline MWs at centimetre scale have been synthesized successfully [31,32,37].

Previous literatures have illustrated that electronic transport of a majority of lead halide perovskites ($APbX_3$) low-dimensional monocrystals are weak and moderate p-type conductivities [44,64,65]. In this context, an ITO conducting glass, which has been deposited a nanofilm of PEDOT:PSS polymer, was featured as the top electrode and transmission window on our proposed photodetection devices [66]. As we previously published, the ITO/PEDOT:PSS glass exhibits excellent electrical properties, and the corresponding transmittances are evaluated averagely to about 80% in the ultraviolet-Visible wavelengths [63,67,68]. Using a commercially available InGaN film substrate as electron transporting medium, a p-n heterojunction photodiode upon a $CsPbBr_3$ MW was produced using an in-situ approach [25,37]. Figure 2(a) depicts a three-dimensional architecture of the photodetection device on account of the hybrid $CsPbBr_3$/InGaN heterostructure composite. In the device, the ITO/PEDOT:PSS glass was served as hole selective layer [66]. Photoelectric tests of the ITO/PEDOT:PSS/$CsPbBr_3$/InGaN device were scientifically performed. Figure 2(b) plots *I*-*V* curve of our fabricated device in the dark, which indicates nonlinear behavior. The inset displays *I*-*V* curves of InGaN film substrate (Ti/Al electrode for the n-type contact) and a single $CsPbBr_3$ MW (ITO/PEDOT:PSS electrode for the p-type contact). The linear behaviors indicate the typical ohmic characteristics of the n- and p-contacts, respectively. Since the contacts are ohmic, the rectifying property of as-fabricated hybrid ITO/PEDOT:PSS/$CsPbBr_3$/InGaN heterostructure is due to the creation of p-n heterojunction between the $CsPbBr_3$ MW and n-type InGaN film substrate. Besides, the lower dark current measured in the negative biasing region could be resulted from the formed high-quality p-n junction. In this case, the diffusion current may be reduced significantly. Conclusively, the $CsPbBr_3$/InGaN heterojunction reveals a standard photodiode characteristics.

The photodiode performances of the $CsPbBr_3$/InGaN heterojunction device were studied. Figure 2(c) exhibits its *I*–*V* curves in logarithmic shape when measured in dark and upon light irradiation with optical wavelengths varying in the scope of 300– 480 nm. With increasing the wavelength from 300 to 400 nm, the recorded photocurrent is going to rise very significantly. As the wavelength exceeds 400 nm, the detected photocurrents exhibit a modest reduce. It suggests that as-constructed $CsPbBr_3$ MW/InGaN photodiode reveals a robust photoresponse properties to the incident lights with their wavelengths in scope of 300–600 nm. Additionally, the photodetection device shows a powerful dependence on photocurrent and a representative photovoltaic effect. The origin of photoresponse characteristics of the $CsPbBr_3$/InGaN photodiode were examined. First, an individual $CsPbBr_3$ monocrystalline wire MSM device was constructed, and a schematic viewpoint of the testing measurement is represented in the inset of Fig. 2(d). In the constructed MSM device, the ITO/PEDOT:PSS glass was used as electrode. The photoelectrical experimentals were conducted in the darkness and illuminating conditions via various wavelengths. Plotted in Fig. 2(d) (the black solid line), the single $CsPbBr_3$ MW exhibits low dark currents, which are smaller than 10^{-10} A. Besides, the observed linear behavior suggests that the ITO/PEDOT:PSS electrode can make ohmic contact with as-synthesized $CsPbBr_3$ samples. Because of the 2.27 eV bandgap, the $CsPbBr_3$ monocrystalline wire reveals a significant photoresponse in a broadband spectrum from ultraviolet ($\sim$ 300 nm) to visible ($\sim$ 600 nm), and realizes the largest photoresponse at a peak wavelength of 405 nm (See Fig. 2(d)). As the device was irradiated ulitizing a 405 nm LED, time-resolved photoresponse of the device shows that the recorded photocurrent can be maintained well at an additional bias voltage of 10.0 V, with well-defined light on/off points and sharp raising/lowering edges, as observed in Fig. 2(e). The measured photocurrent increases gradually with increasing light power intensity [26,32,62]. Second, the electrical and photoelectrical properties of InGaN film were also measured. The device structure on account of

Optics EXPRESS

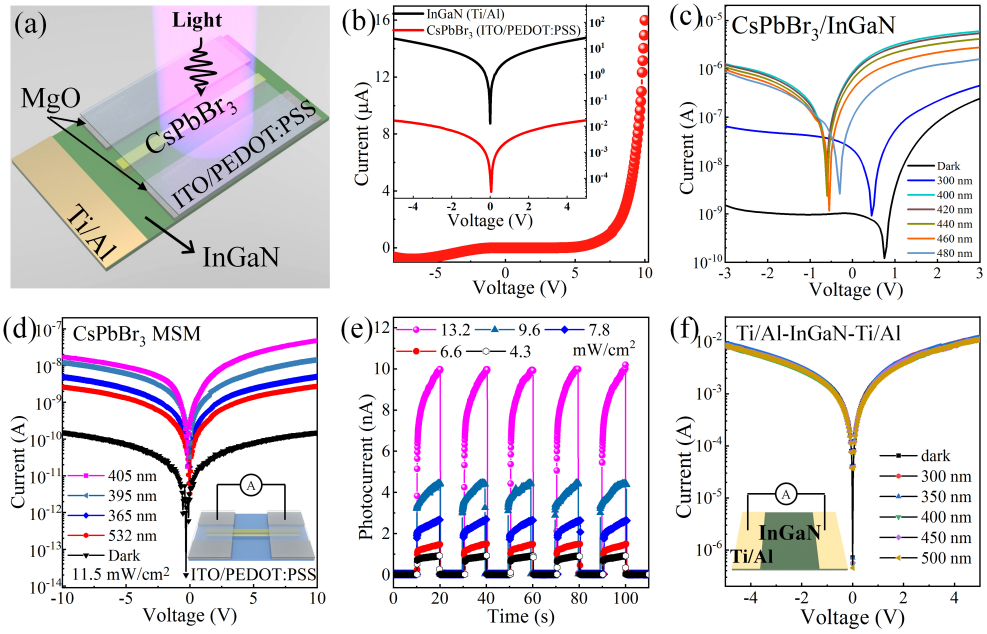

Fig. 2. Characterization of the $CsPbBr_3$ MW/InGaN heterostructure photodetection device. (a) Three-dimensional architecture of as-proposed $CsPbBr_3$ MW/InGaN heterostructure device. (b) *I*–*V* characteristics of the $CsPbBr_3$/InGaN heterostructure device. The inset shows *I*–*V* curves of InGaN film substrate (Ti/Al electrodes) and a single $CsPbBr_3$ MW (ITO/PEDOT:PSS electrodes). (c) *I*–*V* curves of the $CsPbBr_3$ MW/InGaN heterojunction photodiode in the dark and upon light irradiation via various wavelengths ranging from 300 to 480 nm. (d) Semilogarithmic *I*–*V* curves of a single $CsPbBr_3$ MW MSM device in dark and under LED illumination conditions. In the measurement, the wavelengths of illuminated light varied from 365 to 532 nm, and the corresponding optical power densities maintained at 11.5 mW/cm^2. (e) Temporal *I*–*T* curves of the $CsPbBr_3$ MW MSM device upon 405 nm light source irradiation via different light intensities. (f) Semilogarithmic *I*–*V* curves of InGaN film MSM device upon light illumination with different wavelengths (~ 11.5 mW/cm^2).

an InGaN film with Ti/Al electrodes is demonstrated in the inset of Fig. 2(f). Figure 2(f) exhibits the wavelength-dependent *I*–*V* curves (~5.0 mW/cm^2). Distinctly, the InGaN MSM device exhibits no or almost no variability to the light illumination. The photoresponse characteristics of as-constructed $CsPbBr_3$/InGaN photodiode are mainly originated from the p-n heterojunction between weak p-type $CsPbBr_3$ MW and n-InGaN film substrate. Therefore, the as-produced p-$CsPbBr_3$ MW/n-InGaN heterojunction exhibits well-defined rectifying property and much fine light-sensitive features.

Figure 3(a) presents the *I*-*T* curve of the $CsPbBr_3$/InGaN-based photodiode upon light illumination with different wavelengths when measured in a self-biasing manner. Ranging the wavelengths from 300 to 420 nm, the photocurrent dramatically increases. The recorded photocurrent exhibits a prominent decline with increasing the light wavelength in the scope of 420 to 600 nm, which is concerned with the wavelength-dependent absorption properties of as-synthesized $CsPbBr_3$ samples [26,32,62]. The wavelength-dependent photocurrent shows prominent photoresponse in a broadband from ultraviolet to visible, and also acknowledges its largest response to the light wavelength of 420 nm. That is, photoinduced the generation of electron-hole pairs might be effectively separated by the built-in electric field, which has

Optics EXPRESS

been created between $CsPbBr_3$ MW and the underlying InGaN substrate. As the device was illuminated by a 405 nm light source via 5.0 mW/cm^2, time-dependent photoresponse curves were performed at various bias voltages varying from 0 to −4 V. The plotted *I-T* curves in Fig. 3(b) displays that the photocurrents are mostly relied on the applied bias voltages upon the identical illuminating condition. Besides, the device exhibits stable periodic "On" and "Off" switching behaviors. Notably, there is no significant variations in intensity of the obtained photocurrents and photoresponse curves, indicating good and repeatable optical response of the $CsPbBr_3$ MW/InGaN heterojunction photodiode [40–43].

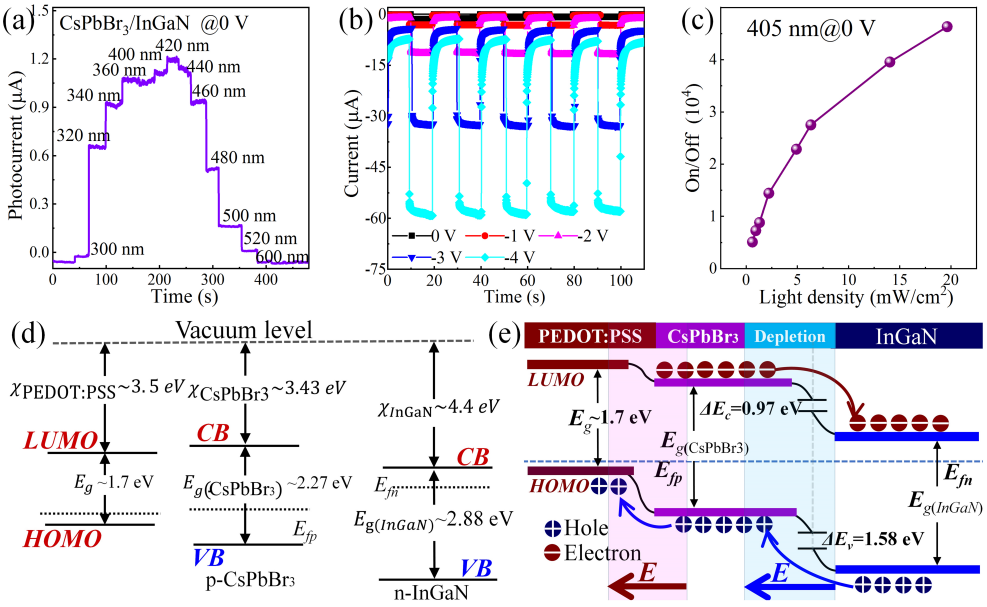

Fig. 3. Photoelectric performances of our constructed $CsPbBr_3$/InGaN photodiode. (a) *I–T* curves of the photodiode upon light irradiation via different wavelengths at 0 V bias. (b) Reverse bias-dependent *I-t* curves recorded in the dark and upon 405 nm LED irradiation (~ 5.0 mW/cm^2). (c) When exposed to the 405 nm LED irradiation at an external biasing voltage of 0 V, the changes of I_{On}/I_{Off} ratio on the incident light intensity. (d) The band scheme of an isolated PEDOT:PSS, $CsPbBr_3$ MW and InGaN film substrate. (e) Schematic energy band diagrams of our constructed $CsPbBr_3$ MW/InGaN photodiode under light illumination at zero bias, so as well as the transsport path of the photogenerated carriers.

Considered that, the photodiode exhibits prominent photovoltaic effect, which enables the $CsPbBr_3$/InGaN heterojunction to be used to construct self-driving photodetectors [22,43]. As the photodiode was irradiated by a 405 nm light source with increasing light power intensities, the photocurrents were recorded at an external biasing voltage of 0 V. Accordingly, the On/Off ratios versus various light power intensities is exhibited in Fig. 3(c). Obviously, inceasing the light power intensity can result in higher value of the On/Off ratio, which can reach a maximum value of 4.6×10^4 at zero biasing voltage. When measured using a much weaker light signal ~ 0.6 mW/cm^2, the On/Off ratio can still be maintained at a high level of 5.0×10^3. This suggests that the represented $CsPbBr_3$/InGaN-based photodiode is extraordinary beneficial to realize light-sensing operation in a self-driving manner. The working principle of as-proposed $CsPbBr_3$/InGaN based photodetector when working in a self-supplying manner was researched. Figure 3(d) represents the energy band structure of the isolated PEDOT:PSS polymer, $CsPbBr_3$ MW, and InGaN film substrate. Shown in the photograph, the electron affinities (χ) of InGaN, $CsPbBr_3$ and PEDOT:PSS are exacted to about 4.4 eV, 3.43 eV and 3.5 eV, respectively [59–61]. The energy

Optics EXPRESS

diagram of ITO/p-PEDOT:PSS/p-$CsPbBr_3$/n-InGaN structure upon thermal equilibrium at an external bias of 0 V is proposed in Fig. 3(e). Since the $CsPbBr_3$ MW being in contact with InGaN film substrate, the difference in Fermi levels would result in the majority carriers interdiffusion between the $CsPbBr_3$ MW (for the hole) and InGaN film substrate (for the electrons). Until the two Fermi levels are aligned, typical type-II heterojunction is observably formed, so as well as the built-in potential created at p-$CsPbBr_3$/n-InGaN heterointerface from InGaN pointing to $CsPbBr_3$ [59,60]. Both the conductivities of PEDOT:PSS and $CsPbBr_3$ are p-type, which indicates that the contact between them creates an p-p heterojunction, thereby holes dominate the conductivity of the structure. Due to the weak p-type behavior of the $CsPbBr_3$ sample, the diffusion movement of holes would occur from PEDOT:PSS to $CsPbBr_3$, giving rise to a space charge region at their interface. A built-in potential could be formed while balancing the drift and diffusion movements for holes at 0 V bias [63]. The direction of $CsPbBr_3$/InGaN built-in potential is clearly in accordance with that of the PEDOT:PSS/$CsPbBr_3$. As the photodetector was illuminated by incoming lights with their energies larger than $E_{g(CsPbBr_3)}$, photocarriers would be mostly produced in the $CsPbBr_3$ sample. Potentially driven by the built-in electric field, the produced electron-holes could be rapidly separated. Particularly for the built-in electric field, which has been formed at the PEDOT:PSS/$CsPbBr_3$ interface, is more conducive to the transport of the photogenerated holes. Currently, the photocarriers can be availably recorded by the electrodes to accomplish the process of photoelectric conversion.

Light irradiation density-dependent photoresponse was carried out upon 405 nm LED irradiation at an additional bias of 0 V. Figure 4(a) exhibits dynamic photoresponse, which is principally relied on light power densities of 405 nm LED. Shown in the photograph, the photoresponse exhibits an approximately linear increase, thus achieving a maximum photocurrent of 1.45 μA at 4.904 mW/cm^2. The obtained photocurrent exhibits a positive dependence on the power density of the incident light. That is, the higher light intensity would lead to more photogenerated carriers in the active region, thus yielding larger photocurrent. Besides, the detector demonstrates excellent photovoltaic cycling stability. Switching the incoming light between on and off states, the photodiode displays an alternating occurrence of photocurrent and dark current, which maintains a few cycles. The variation of the photocurrent relating to the light intensity for our constructed $CsPbBr_3$ MW/InGaN heterojunction device is depicted in Fig. 4(b). According to law formula $I_{ph} = AP^{\theta}$, the relationship between photocurrent and the light power density was fitted. In the formula, A, P and θ are a constant, light power density, and the index of power law, respectively. The θ was evaluated to about 0.91, which indicates much lower traps and interfacial defect states in the as-synthesized $CsPbBr_3$ monocrystalline MWs and the relating $CsPbBr_3$/InGaN heterojunction device. A single-period response was then shown in Fig. 4(c). The response and recover speed, which are resulted from the time interval varying between 10 and 90% of the largest photocurrent, are evaluated to be less than 1.9/0.06 s, respectively.

The key figures of merit of the photodetectors, which are made of photoresponsivity (R), detectivity (D^*), external quantum efficiency (EQE) and linear dynamic range (LDR), are further evaluated. These parameters are directly related to the photoresponse ability of photodetectors. First, the R is derived from the equation:

$$R = \frac{I_{ph} - I_d}{P_{in}S}. \tag{1}$$

In the equation, I_{ph} is the measured current as the light is turned on, I_d is the recorded current in the darkness, P_{in} is identified as optical power density of the irradiated light, and S is recognized as the resultful irradiation area ($\sim 8\times10^{-4}$ cm^2). The specific detectivity D^* is deduced to being

$$D^* = \frac{R\sqrt{S}}{\sqrt{2qI_d}}. \tag{2}$$

Optics EXPRESS

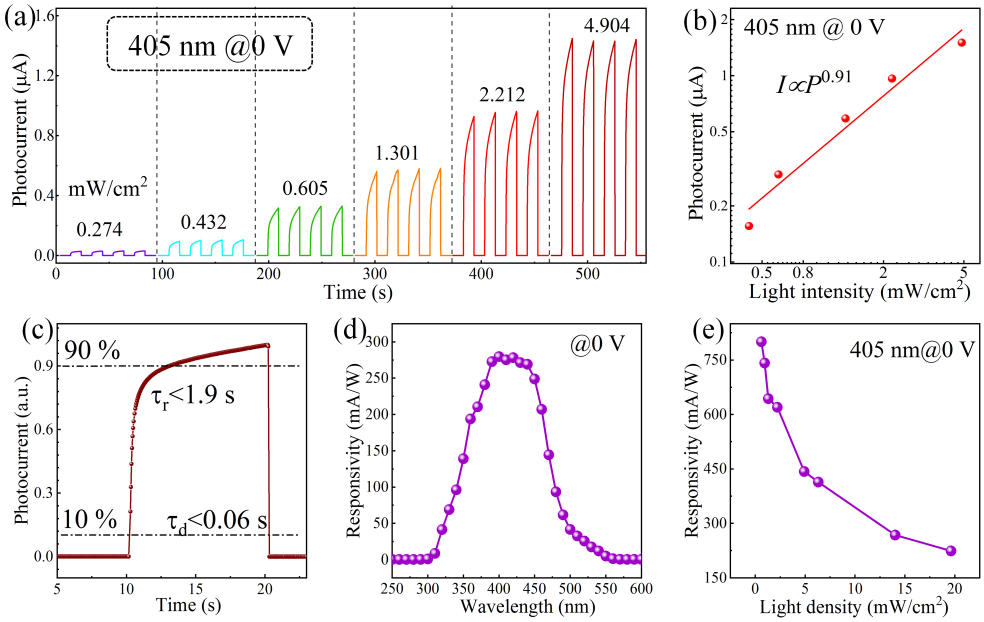

Fig. 4. Photoresponse properties of as-proposed $CsPbBr_3$/InGaN photodiode. (a) Photocurrent switching performances upon 405 nm LED irradiation via various lighting densities when tested in a self-powered manner. (b) When illuminated using a 405 nm LED, the recorded photocurrent versus the incident intensity at 0 V bias, and a nearly ideal power exponent was fitted approximately to be 0.91. (c) Time-resolved photoresponse, the rise (τ_r) and decay (τ_d) times are approximately less than 1.9 s and 0.06 s, respectively. (d) Wavelength-dependent photoresponsivity at zero bias. (e) Light irradiation power-dependent responsivity at zero bias.

In the expression, R and q describe the spectral responsivity and the basic charge, respectively. The EQE, determining the conversion efficiency of light to electricity for the photodetection devices, is actually defined the photoresponse properties. The EQE might be expressed using the formula:

$$EQE = \frac{Rhc}{e\lambda}. \tag{3}$$

Wherein λ, h and c are respectively named the optical wavelength of incident light, Planck constant, and the speed of light. The LDR, which defines the signal/noise ratio, is expressed using the below formula:

$$LDR = 20 \log \frac{I_{ph}}{I_d}. \tag{4}$$

Considering our $CsPbBr_3$/InGaN heterojunction detector, the calculated spectral responsivity curves, which is dependent on the light wavelengths, is plotted in Fig. 4(d). The fabricated heterojunction photodetector can reach its largest response of 281.5 mA/W at 405 nm. The bandwidth of the photodetection band is evaluated to about 150 nm. Thus, the photosensitive characteristics of as-constructed $CsPbBr_3$/InGaN heterojunction device is intact over a wide wavelength spectrum, signifying its wide-band photodetection capability. Particularly, the device illustrates much weaker photoresponse as the light wavelength varies lower than 300 nm and larger than 600 nm. In the down-to-earth applications, the light absorption in a broadband wavelengths, which is combined with excellent photosensitive properties, has a profound significance for withdrawing and detecting photons of the specific wavelengths. Figure 4(e) represents the

Optics EXPRESS

illumination intensity-dependent responsivity of the photodiode at 405 nm. In this cases, the responsivity exhibits a negative dependence on the incident light intensity. The largest value of responsivity ~ 800.0 mA/W is achieved at the light intensity of 0.605 mW/cm^2.

We further examined the photoresponse properties of the $CsPbBr_3$ MW/InGaN heterojunction photodetector when characterized in a self-driving mode. The D^* is crucially important index for the photodetector. The wavelength-dependent D^*, which is checked at 0 V bias, is firstly plotted in Fig. 5(a). The largest D^* value of 1.35×10^{12} Jones could be achieved at 405 nm, which has been computed using the Eq. (2). Accordingly, the changes of D^* in terms of light irradiation intensity is shown in Fig. 5(b), which exhibits a negative relationship. The D^* might reach the highest value of 4.6×10^{12} Jones as the light irradiation intensity is reduced to 0.605 mW/cm^2. The EQE, which is plotted as a function of light wavelength at 0 V bias, is displayed in Fig. 5(c). The EQE value can reach a maximum value of about 86.5%, showing a preferable photoresponse performance at λ=405 nm. Figure 5(d) plots EQE versus incident light intensity. Notably, the EQE values have slipped significantly with increasing light intensity, which manifested that the recombination loss cannot be ignored at high light intensity in the $CsPbBr_3$ MW/InGaN based photodiode. Finally, the wavelength-dependent LDR of the detector is depicted in Fig. 5(e). The largest LDR value is extracted to about 64.5 at 405 nm at 0 V biasing condition. The variation of LDR on light irradiation intensity is exhibited in Fig. 5(f). Increasing the optical intensity of the illuminated light, the LDR illustrates a significant increase varying from 74.0 to 93.9. Overall, these photoresponse performances are highly competitive or even more powerful than those of already published low-dimensional $CsPbBr_3$-based self-powered photodetectors and Si-based photodetectors with relating device geometries.

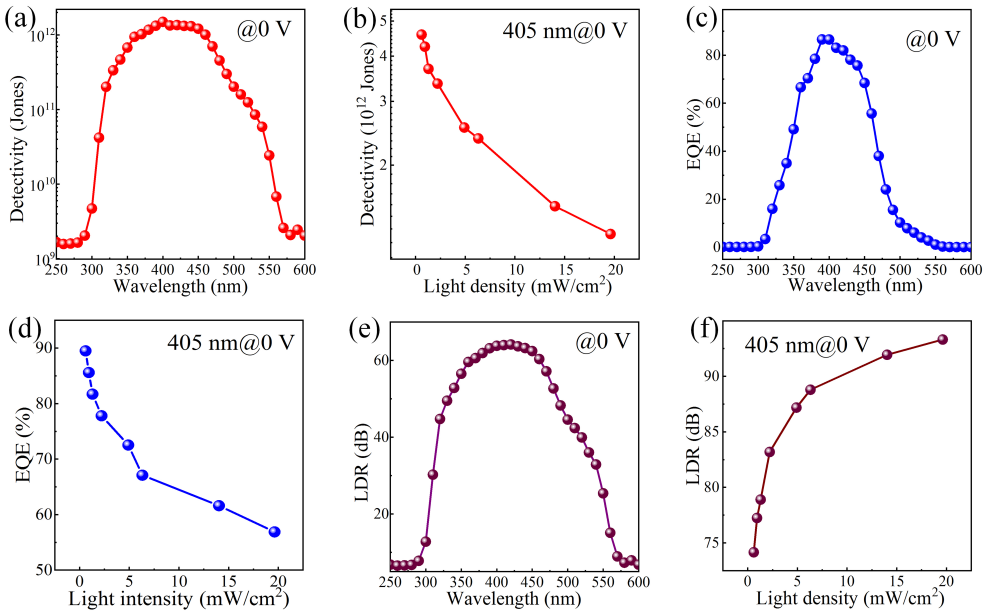

Fig. 5. Photoresponse behaviors of the $CsPbBr_3$/InGaN-based photodiode. (a) The change of detectivity on the light wavelengths when tested at zero bias. (b) Light illumination density-dependent detectivity of the photodiode at 0 V bias (Light wavelength ~ 405 nm). (c) The change of EQE on the light wavelengths at zero bias voltage. (d) Light illumination density-dependent EQE at zero bias voltage. (e) Wavelength-dependent LDR at zero bias voltage. (f) Light illumination density-dependent LDR of the photodiode at zero bias.

Optics EXPRESS

To access the actual response speed, an experiment was performed using a nanosecond pulsed laser as the ultrafast light source (λ_{ex}=405 nm, pulse width 5 ns, 10 Hz). The resulting setup is schematically shown in Fig. 6(a). In which, a digital oscilloscope was employed to detect the temporal photoresponse signal (photovoltage against time). Figure 6(b) shows the time-resolved photoresponse performances. Thus, the device exhibits much fast response speed and good repeatability after nine cycles. An enlarged view response is further exhibited in Fig. 6(c). To examine the photoresponse speed, the transient response curve was numerically fitted using a double exponential relaxation equation of $y = y_0 + A_1 e^{-t/\tau_1} + A_2 e^{-t/\tau_2}$. In the formula, y_0 is the steady-state photocurrent, t is time, A_1 and A_2 are constants, and τ_1 and τ_2 are the relaxation time constants, which correspond to two components [63,67,68]. In general, the fast-response constituent is connected with the rapid change of carrier concentration as the light is turned on/off. While the slow-response constituent is strongly associated with carrier capturing/releasing, which are derived from surface and interface defects. Accordingly, the rising/falling times are evaluated to be 4.48 ms and 7.68 ms, respectively. The result indicates that as-proposed ITO/PEDOT:PSS/$CsPbBr_3$/InGaN heterojunction photodiode possesses the potential to catch light signals in the ultraviolet-visible wavelengths at a terrific speed. The photodetection properties of as-constructed $CsPbBr_3$ MW/InGaN heterojunction device were compared with previously reported literature, which were fabricated on account of low-dimensional $CsPbBr_3$ nano- and microcrystals heterojunctions, seen Table 1. Our demonstrated photodetectors in the present study exhibit a better photosensing properties, especially in the spectral responsivity, specific detecivity, and response speed.

Table 1. Comparison of the performance metrics of low-dimensional $CsPbBr_3$ heterojunction photodetectors.

Photodetector	Bias	On/off ratio	Responsivity	D*(Jones)	Response time	Ref.
$CsPbBr_3$ MW	5 V	3.57×10^3	312.2 A/W	1.5×10^{13}	20/5.8 ms	[69]
Ag@$CsPbBr_3$ MW	3 V	$\sim10^5$	18.96 A/W	1.67×10^{14}	17 ms/57 ms	[62]
$CsPbBr_3$ MW	5 V	$\sim10^3$	118 A/W	$>10^{12}$	<40 ms	[50]
$CsPbBr_3$/GaN	10 V	$\sim10^2$	1.78 A/W	6.5×10^{13}	13.5 s/2.7 s	[60]
$CsPbBr_3$/ZnO	−5 V	–	626 μA/W	7×10^9	61 μs/1.4 ms	[40]
WS_2/$CsPbBr_3$ vdWH	2 V	$\sim10^{9.83}$	57.2 A/W	1.36×10^{14}	~2 ms	[57]
$CsPbBr_3$ NW	0 V	$\sim10^6$	0.3 A/W	1.0×10^{13}	0.4/0.43 ms	[49]
Se microtube/$CsPbBr_3$	0 V	235	47.6 mA/W	4.9×10^{10}	18/40 ms	[53]
$CsPbBr_3$:ZnO QDs	0 V	$\sim10^2$	0.24 mA/W	–	680 ns/436 μs	[55]
$CsPbBr_3$ nanonet/SnO_2	0 V	1.35×10^6	190 mA/W	4.31×10^{12}	0.06 ms/0.26 ms	[48]
Au/$CsPbBr_3$ microplate	0 V	$> 10^6$	200 mA/W	$\sim10^{12}$	75/70 μs	[47]
$CsPbBr_3$ Nanonet	0 V	4.17×10^4	91.46 mA/W	7.44×10^{11}	0.1/0.16 ms	[58]
$CsPbBr_3$ MW/InGaN	0 V	4.6×10^5	800 mA/W	4.6×10^{12}	4.48 ms/7.68 ms	This work

Device stability and reliability are the essential parameters in the practical application. When worked in a self-biasing manner, the stability and repeatability of as-constructed $CsPbBr_3$ MW/InGaN heterojunction photodetector were performed upon a 405 nm LED illumination via 5.0 mW/cm^2. As seen in Fig. 6(d), the values of recorded photocurrents could be regarded as a constant without any encapsulation when operated in a self-biasing mode through maintaining 200 cycles. This observation exhibits that the photodiode presented in this paper possesses fantastic photostability and long-term operational stability. Besides, the switching result reveals a great repeatability and ultrafast photoresponse times. The long-term stability was further tested. The dark-current and photocurrent versus storage time were recorded periodically under a 405 nm LED illumination at 0 V bias (~ 5.0 mW/cm^2). During the measurement, the photodiode

Optics EXPRESS

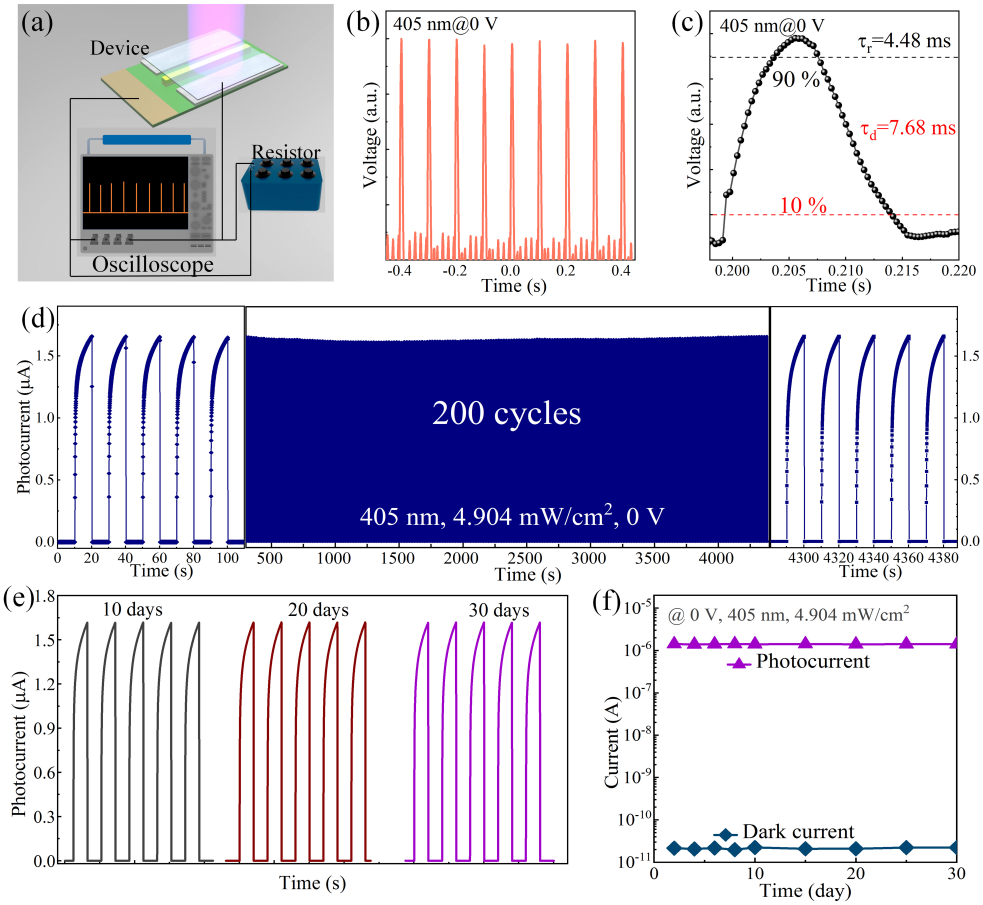

Fig. 6. Transient response speed and long-term stability measurements of as-proposed $CsPbBr_3$/InGaN photodiode. (a) Schematic of the instrumentation system for transient photoresponse measurement under 405 nm pulse laser illumination when tested in a self-biasing operation manner. (b) The transient photoresponse result. (c) The evaluated rising/decaying times from a single pulse response curve. (d) Long-term photoresponse curve of the photodetector without any encapsulation under 405 nm LED irradiation via 5.0 mW/cm^2. (e) The *I*–*t* curve of the $CsPbBr_3$/InGaN heterojunction photodetector after 10, 20 and 30 days of storage in air atmosphere. (f) The variation of recorded photocurrent as a function of storage duration.

Optics EXPRESS

without any encapsulation was stored in a laboratory conditions under ambient conditions (Temperature −5 ~ 30°, Humidity~ 50%), and the device was measured in the uninterrupted measurement. As illustration in Figs. 6(e) and (f), the results reveal that even after 30 days, the device remains highly sensitive to the light signals and demonstrated a negligible changes of the peak photocurrents, suggesting the outstanding long-term stability of as-proposed $CsPbBr_3$ MW/InGaN heterojunction self-powered photodetector. Therefore, benefiting from the fine stabilities of chemical and physical properties of InGaN films, the photodetectors demonstrate outstanding reliability and stability.

As a potential application, the photoimaging performances of as-fabricated $CsPbBr_3$ MW/InGaN heterojunction device was tested in a self-driving operation manner. Using the photodetector as a sensing pixel, an imaging measurement setup was constructed. The system via optical path is schematically shown in Fig. 7(a). In the experimental setup, the hollow letters "U" and "V", which are derived from the abbreviation of ultraviolet and visible, were made on a piece of black mask plate. The mask plate can be moved in horizontal and vertical directions (x–y direction) using a two-dimensional translation stage, which is controlled using a computer. The position-dependent current generated using the photodetector flows through external circuit, and then could be recorded using the B1500A in real time. Along with the scanning of the translation stage, the photocurrents and the position coordinates of the object were recorded using the computer simultaneously. In the imaging measurement, the LEDs emitting at the light wavelengths of 350, 405 and 530 nm were adopted as the ultraviolet-visible light sources. During

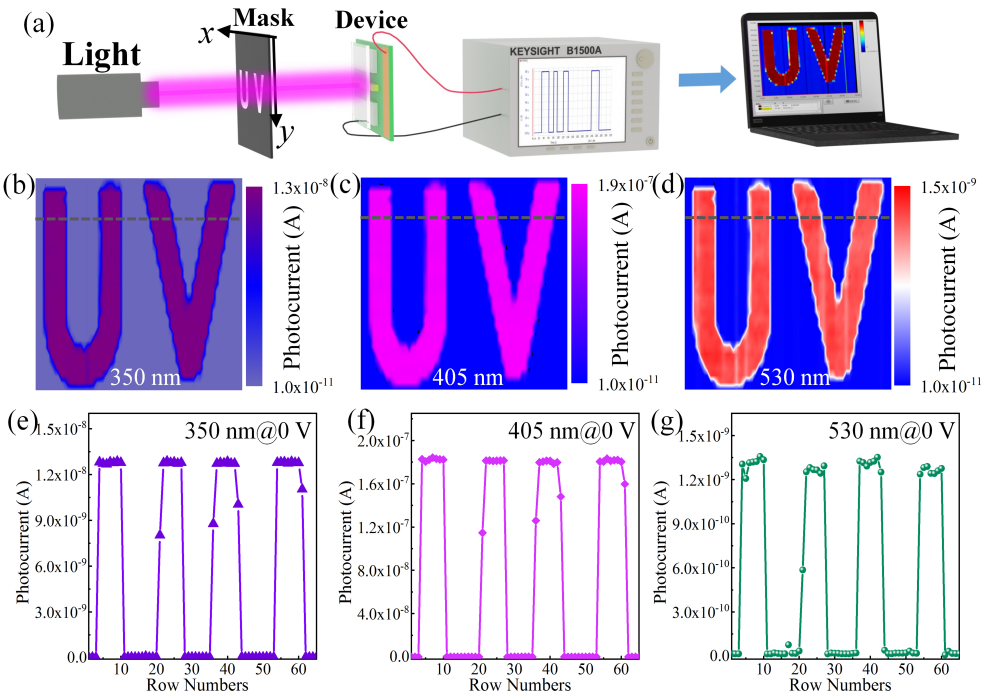

Fig. 7. Photosensing capability of our constructed $CsPbBr_3$ MW/InGaN heterojunction photodetection device. (a) Schematic view of the testing system for single-pixel imaging measurement. When measured in a self-driving manner, the obtained imaging results of the ultraviolet ("U") and visible ("V") pattern under light illumination at wavelength of (b) 350 nm, (c) 405 nm and (d) 530 nm, respectively. (e)-(g) Signal detected photocurrent along the pre-marked dotted line in (b), (c) and (d).

Optics EXPRESS

the test, the light intensities of the used LED light sources maintained at a constant value ~ 0.5 mW/cm^2. Under light illumination, the shape letters "U V" are factually imaged. Figures 7(b)-(d) exhibit three photographs created using the obtained position information and corresponding electrical signal values. Clearly, the imaging targets "U V" were obtained using the mask plate without any external power supply. The imaged shape letters with sharp boundaries are obtained with low background. Due to the wavelength-dependent photosensing properties, the obtained shape letters illustrate obvious difference in color imaging. Besides, the measured photocurrents of the imaginary line are depicted in Figs. 7(e)-(g), respectively. The sharp changes of the photocurrents at the letter boundaries are consistent with the imaging target. The obtained photographs and the objects are similar, indicating that as-constructed $CsPbBr_3$ MW/InGaN heterojunction photodetector can be utilized as a photosensing pixel to acquire high-fidelity images through photodetection of ultraviolet-visible light without an external power supply.

4. Conclusions

To summarize, we exhibited a facile and cost-effective route to construct a hybrid perovskite/InGaN heterostructure toward the realization of self-powered, broadband and highly-sensitive photodetectors. The in-situ fabricated and non-encapsulated photodetector exhibited a simple device architecture to realize an air-stable photosensitive capabilities with competitive performances by comparing with other perovskite-related materials and optoelectronic devices. Benefitting from the strong absorption of the $CsPbBr_3$ MWs and efficient interface charge transfer caused by the favorable $CsPbBr_3$ MW/InGaN heterojunction, the device demonstrated fantastic photodetection performances with a largest responsivity of 800.0 mA/W, a maximum detectivity ~ 4.6×10^{12} Jones, and high EQE approaching 89.5% under 405 nm light irradiation in a self-driving manner. The response speed is ultrafast with the raising/falling times of 4.48 ms/7.68 ms. The excellent photoresponse is mainly resulted from the in-situ constructed $CsPbBr_3$/InGaN heterojunction, along with the additional built-in electric field at ITO/PEDOT:PSS-$CsPbBr_3$ interface, which could promote the photogenerated holes transfer. Thereby, the ITO/PEDOT:PSS-$CsPbBr_3$/InGaN heterojunction can achieve effectively suppression of photocarrier non-recombination and accelerate carriers transfer. Further, the self-powered photodetector featuring as a photosensing pixel can be used to achieve high uniformity, high spatial resolution and clear images, determining its broadband imaging capability. Overall, using an in situ, low-budget, simple-structure and mass production, the finding opens a new pathway to design low-dimensional all-inorganic halide perovskites heterojunction optoelectronic devices toward practical application in future.

Funding. Project of Innovation and Entrepreneurship Training for National College Students in Henan Province (202210478009); Key Scientific Research Project of Colleges and Universities in Henan Province (22A140033); Natural Science Foundation of Henan Province (232300421222); Fundamental Research Funds for the Central Universities (NC2022008); National Natural Science Foundation of China (11974182, 12374257).

Disclosures. The authors declare that there are no conflicts of interest related to this article.

Data availability. The data underlying the results presented in this paper are not publicly available at this time but may be obtained from the authors upon reasonable request.

References

1. Q. Mo, C. Chen, W. Cai, *et al.*, "Room Temperature Synthesis of Stable Zirconia-Coated $CsPbBr_3$ Nanocrystals for White Light-Emitting Diodes and Visible Light Communication," Laser Photonics Rev. **15**(10), 2100278 (2021).
2. S. Zhao, Q. Mo, B. Wang, *et al.*, "Inorganic halide perovskites for lighting and visible light communication," Photonics Res. **10**(4), 1039–1062 (2022).
3. L. N. Quan, B. P. Rand, R. H. Friend, *et al.*, "Perovskites for next-generation optical sources," Chem. Rev. **119**(12), 7444–7477 (2019).
4. X. Ye, C. Li, J. Jiang, *et al.*, "Morphology dependent light–induced photoluminescence enhancement of $CsPbBr_3$ microcrystals," Chem. Commun. **59**(23), 3403–3406 (2023).
5. I. Metcalf, S. Sidhik, H. Zhang, *et al.*, "Synergy of 3D and 2D perovskites for durable, efficient solar cells and beyond," Chem. Rev. **123**(15), 9565–9652 (2023).

Optics EXPRESS

6. Z. Xu, X. Han, W. Wu, *et al.*, "Controlled on-chip fabrication of large-scale perovskite single crystal arrays for high-performance laser and photodetector integration," Light: Sci. Appl. **12**(1), 67 (2023).
7. H. Xiao, J. Fu, X. Wei, *et al.*, "Photoelectron-extractive and ambient-stable $CsPbBr_3$@SnO_2 nanocrystals for high-performance photodetection," Laser Photonics Rev. **16**(11), 2200276 (2022).
8. H. Guan, S. Zhao, H. Wang, *et al.*, "Room temperature synthesis of stable single silica-coated $CsPbBr_3$ quantum dots combining tunable red emission of Ag-In-Zn-S for High-CRI white light-emitting diodes," Nano Energy **67**, 104279 (2020).
9. S. Zhao, Z. Jia, Y. Huang, *et al.*, "Solvent-Free Synthesis of Inorganic Rubidium Copper Halides for Efficient Wireless Light Communication and X-Ray Imaging," Adv. Funct. Mater. **33**, 2305858 (2023).
10. H. Wang, M. Yang, W. Cai, *et al.*, "Suppressing Phase Segregation in $CsPbIBr_2$ Films via Anchoring Halide Ions toward Underwater Solar Cells," Nano Lett. **23**(10), 4479–4486 (2023).
11. J. Deng, J. Li, Z. Yang, *et al.*, "All-inorganic lead halide perovskites: a promising choice for photovoltaics and detectors," J. Mater. Chem. C **7**(40), 12415–12440 (2019).
12. H. Wang and D. H. Kim, "Perovskite-based photodetectors: materials and devices," Chem. Soc. Rev. **46**(17), 5204–5236 (2017).
13. N. Ding, Y. Wu, W. Xu, *et al.*, "A novel approach for designing efficient broadband photodetectors expanding from deep ultraviolet to near infrared," Light: Sci. Appl. **11**(1), 91 (2022).
14. A. Liu, H. Zhu, S. Bai, *et al.*, "High-performance inorganic metal halide perovskite transistors," Nat. Electron. **5**(2), 78–83 (2022).
15. M. Tan, M. Li, W. Pan, *et al.*, "Carbonized polymer dots enhanced stability and flexibility of quasi-2D perovskite photodetector," Light: Sci. Appl. **11**(1), 304 (2022).
16. Y. Zhong, K. Liao, W. Du, *et al.*, "Large-scale thin $CsPbBr_3$ single-crystal film grown on sapphire via chemical vapor deposition: Toward laser array application," ACS Nano **14**(11), 15605–15615 (2020).
17. J. Liu, J. Jin, Z. Yang, *et al.*, "Extremely low program current memory based on self-assembled all-inorganic perovskite single crystals," ACS Appl. Mater. Interfaces **12**(28), 31776–31782 (2020).
18. S. Yan, S. Tang, M. Luo, *et al.*, "Surface passivation by congeneric quantum dots for high-performance and stable $CsPbBr_3$-based photodetectors," J. Mater. Chem. C **9**(31), 10089–10100 (2021).
19. X. Liu, X. Tan, Z. Liu, *et al.*, "Enhancing the performance of all vapor-deposited electron-conductor-free $CsPbBr_3$ photodetectors via interface engineering for their applications in image sensing," J. Mater. Chem. C **8**(41), 14409–14422 (2020).
20. Z. Gu, Y. Zhao, Y. Zhang, *et al.*, "Ion aggregation-induced crystallization strategy for printing morphology-controllable perovskite single-crystal arrays and integrated devices," Chem. Mater. **35**(13), 5127–5134 (2023).
21. C. H. Kang, I. Dursun, G. Liu, *et al.*, "High-speed colour-converting photodetector with all-inorganic $CsPbBr_3$ perovskite nanocrystals for ultraviolet light communication," Light: Sci. Appl. **8**(1), 94 (2019).
22. C. Tian, F. Wang, Y. Wang, *et al.*, "Chemical vapor deposition method grown all-inorganic perovskite microcrystals for self-powered photodetectors," ACS Appl. Mater. Interfaces **11**(17), 15804–15812 (2019).
23. L. Mei, K. Zhang, N. Cui, *et al.*, "Ultraviolet–visible–short–wavelength infrared broadband and fast–response photodetectors enabled by individual monocrystalline perovskite nanoplate," Small **19**(37), 2301386 (2023).
24. S. Pal, A. Ghorai, S. Mahato, *et al.*, "Piezo-phototronic effect-induced self-powered broadband photodetectors using environmentally stable α-$CsPbI_3$ perovskite nanocrystals," Adv. Opt. Mater. **11**(16), 2300233 (2023).
25. L. Ma, Y. Tan, W. Zhou, *et al.*, "In-situ strain engineering on the emission and photoresponse of epitaxial vertical and horizontal $CsPbBr_3$ triangular nanoplates," Mater. Lett. **315**, 131931 (2022).
26. D. Li, Y. Meng, Y. Zhang, *et al.*, "Selective surface engineering of perovskite microwire arrays," Adv. Funct. Mater. **33**(33), 2302866 (2023).
27. M. Wang, F. Cao, L. Li, *et al.*, "Metal halide perovskite nano/microwires," Small Struct. **3**(1), 2100165 (2022).
28. Y. Yang, F. Gao, Q. Liu, *et al.*, "Long and ultrastable all-inorganic single-crystal $CsPbBr_3$ microwires: One-step solution in-plane self-assembly at low temperature and application for high-performance photodetectors," J. Phys. Chem. Lett. **11**(17), 7224–7231 (2020).
29. Z. Lai, Y. Meng, F. Wang, *et al.*, "PDMS-assisted low-temperature synthesis of submillimeter all-inorganic halide perovskite microcrystals for high-performance photodetectors," Adv. Opt. Mater. **10**(20), 2201127 (2022).
30. S. Wang, K. Wang, Z. Gu, *et al.*, "Solution-phase synthesis of cesium lead halide perovskite microrods for high-quality microlasers and photodetectors," Adv. Opt. Mater. **5**(11), 1700023 (2017).
31. G. Tong, M. Jiang, D.-Y. Son, *et al.*, "2D Derivative Phase Induced Growth of 3D all inorganic perovskite micro–nanowire array based photodetectors," Adv. Funct. Mater. **30**(34), 2002526 (2020).
32. Z. Yang, M. Jiang, L. Guo, *et al.*, "A high performance $CsPbBr_3$ microwire based photodetector boosted by coupling plasmonic and piezo-phototronic effects," Nano Energy **85**, 105951 (2021).
33. F. Ma, Z. Huang, M. Zioek, *et al.*, "Template-assisted synthesis of a large-area ordered perovskite nanowire array for a high-performance photodetector," ACS Appl. Mater. Interfaces **15**(9), 12024–12031 (2023).
34. Y. Wei, X. Liu, Y. Miao, *et al.*, "A high-responsivity $CsPbBr_3$ nanowire photodetector induced by CdS@$Cd_xZn_{1-x}S$ gradient-alloyed quantum dots," Nanoscale Horiz. **7**(6), 644–654 (2022).
35. N. Jiang, J. Wei, M. Lv, *et al.*, "Phase evolution and fluorescence stability of $CsPb_2Br_5$ microwires and their application in stable and sensitive photodetectors," J. Mater. Chem. C **11**(18), 6046–6056 (2023).

Optics EXPRESS

36. C. Chen, Z. Li, L. Fu, *et al.*, "Perovskite photodetector-based single pixel color camera for artificial vision," Light: Sci. Appl. **12**(1), 77 (2023).
37. C. Lin, P. Wan, B. Yang, *et al.*, "Plasmon-enhanced photoresponse and stability of a $CsPbBr_3$ microwire/GaN heterojunction photodetector with surface-modified Ag nanoparticles," J. Mater. Chem. C **11**(38), 12968–12980 (2023).
38. W. Wu, H. Lu, X. Han, *et al.*, "Recent progress on wavelength-selective perovskite photodetectors for image sensing," Small Methods **7**(4), 2201499 (2023).
39. Y. Zou, T. Zou, C. Zhao, *et al.*, "A highly sensitive single crystal perovskite–graphene hybrid vertical photodetector," Small **16**(25), 2000733 (2020).
40. L. Su, T. Li, Y. Zhu, *et al.*, "A vertical $CsPbBr_3$/ZnO heterojunction for photo-sensing lights from UV to green band," Opt. Express **30**(13), 23330–23340 (2022).
41. W. Hu, H. Cong, W. Huang, *et al.*, "Germanium/perovskite heterostructure for high-performance and broadband photodetector from visible to infrared telecommunication band," Light: Sci. Appl. **8**(1), 106 (2019).
42. W. Gong, J. Yan, F. Gao, *et al.*, "High-performance UV–Vis Broad–Spectra Photodetector Based on a β-Ga_2O_3/Au/$MAPbBr_3$ sandwich structure," ACS Appl. Mater. Interfaces **14**(42), 47853–47862 (2022).
43. B. Yang, P. Guo, D. Hao, *et al.*, "Self-powered photodetectors based on $CsPbBr_3$ quantum dots/organic semiconductors/SnO_2 heterojunction for weak light detection," Sci. China Mater. **66**(2), 716–723 (2023).
44. S. Liu, Y. Chen, W. Gao, *et al.*, "Epitaxy of a monocrystalline $CsPbBr_3$–$SrTiO_3$ halide–oxide perovskite p–n heterojunction with high stability for photodetection," Adv. Mater. **35**(31), 2303544 (2023).
45. H. Cong, X. Chu, F. Wan, *et al.*, "Broadband photodetector based on inorganic perovskite $CsPbBr_3$/GeSn heterojunction," Small Methods **5**(8), 2100517 (2021).
46. J. Liu, F. Liu, H. Liu, *et al.*, "Mixed-dimensional $CsPbBr_3$@ZnO heterostructures for high-performance p-n diodes and photodetectors," Nano Today **36**, 101055 (2021).
47. P. Gui, J. Li, X. Zheng, *et al.*, "Self-driven all-inorganic perovskite microplatelet vertical schottky junction photodetectors with a tunable spectral response," J. Mater. Chem. C **8**(20), 6804–6812 (2020).
48. H. Zhou, R. Wang, X. Zhang, *et al.*, "Ionic liquid enables high-performance, self-powered $CsPbBr_3$ perovskite nanonet photodetector," Chem. Commun. **59**(55), 8544–8547 (2023).
49. H. Zhou, Z. Song, C. R. Grice, *et al.*, "Self-powered $CsPbBr_3$ nanowire photodetector with a vertical structure," Nano Energy **53**, 880–886 (2018).
50. P. Gui, Z. Chen, B. Li, *et al.*, "High-performance photodetectors based on single all-inorganic $CsPbBr_3$ perovskite microwire," ACS Photonics **5**(6), 2113–2119 (2018).
51. R. Xing, P. Shi, D. Wang, *et al.*, "Flexible self-powered weak light detectors based on ZnO/$CsPbBr_3$/γ-CuI heterojunctions," ACS Appl. Mater. Interfaces **14**(35), 40093–40101 (2022).
52. F. Wang, H. Zhang, X. Song, *et al.*, "High–responsivity Vis–NIR photodetector based on a Ag_2S/$CsPbBr_3$ heterojunction," ACS Appl. Electron. Mater. **4**(8), 3922–3929 (2022).
53. T. Zheng, Q. Du, W. Wang, *et al.*, "High performance and self-powered photodetectors based on Se/$CsPbBr_3$ heterojunctions," J. Mater. Chem. C **11**(11), 3841–3847 (2023).
54. Y. Li, Z. Shi, L. Lei, *et al.*, "Controllable vapor-phase growth of inorganic perovskite microwire networks for high-efficiency and temperature-stable photodetectors," ACS Photonics **5**(6), 2524–2532 (2018).
55. W. Gong, Y. Tian, J. Yan, *et al.*, "Performance enhancement of a self-powered imaging $CsPbBr_3$ photodetector by tuning the trap effects of carriers," J. Mater. Chem. C **10**(19), 7460–7468 (2022).
56. X. Zhan, X. Zhang, Z. Liu, *et al.*, "Boosting the performance of self-powered $CsPbCl_3$-Based UV photodetectors by a sequential vapor-deposition strategy and heterojunction engineering," ACS Appl. Mater. Interfaces **13**(38), 45744–45757 (2021).
57. Q. Xu, Z. Yang, D. Peng, *et al.*, "WS_2/$CsPbBr_3$ van der Waals heterostructure planar photodetectors with ultrahigh on/off ratio and piezo-phototronic effect-induced strain-gated characteristics," Nano Energy **65**, 104001 (2019).
58. R. Wang, H. Zhou, B. Wu, *et al.*, "Self-powered $CsPbBr_3$ perovskite nanonet photodetector with a hollow vertical structure," J. Phys. Chem. Lett. **12**(31), 7519–7525 (2021).
59. J. Zhang, B. Jiao, J. Dai, *et al.*, "Enhance the responsivity and response speed of self-powered ultraviolet photodetector by GaN/$CsPbBr_3$ core-shell nanowire heterojunction and hydrogel," Nano Energy **100**, 107437 (2022).
60. L. Su, Y. Zhang, J. Xie, *et al.*, "An all-inorganic $CsPbBr_3$/GaN hetero-structure for a near UV to green band photodetector," J. Mater. Chem. C **10**(4), 1349–1356 (2022).
61. L. Luo, Y. Huang, K. Cheng, *et al.*, "MXene-GaN van der Waals metal-semiconductor junctions for high performance multiple quantum well photodetectors," Light: Sci. Appl. **10**(1), 177 (2021).
62. B. Hanqi, M. Jiang, C. Lin, *et al.*, "Flexible $CsPbBr_3$ microwire photodetector with a performance enhanced by covering it with an Ag nanolayer," CrystEngComm **24**(43), 7620–7631 (2022).
63. Q. Li, Y. Liu, X. Guan, *et al.*, "High-performance ultraviolet photodetector based on p-PEDOT:PSS film/p-ZnO:Sb microwire/n-Si double heterojunction," Ceram. Int. **49**(5), 8302–8312 (2023).
64. Y. Feng, L. Pan, H. Wei, *et al.*, "Low defects density $CsPbBr_3$ single crystals grown by an additive assisted method for γ-ray detection," J. Mater. Chem. C **8**(33), 11360–11368 (2020).
65. X. Du, Y. Liu, W. Pan, *et al.*, "Chemical Potential Diagram Guided Rational Tuning of Electrical Properties: A Case Study of $CsPbBr_3$ for X-ray Detection," Adv. Mater. **34**(17), 2110252 (2022).

Optics EXPRESS

66. Y. Lin, J. Zou, W. Wang, *et al.*, "High-performance self-powered ultraviolet photodetector based on PEDOT:PSS/CuO/ZnO nanorod array sandwich structure," Appl. Surf. Sci. **599**, 153956 (2022).
67. Y. Liu, M. Jiang, P. Wan, *et al.*, "Enhanced performance of ZnO microwire/PEDOT:PSS heterojunction ultraviolet photodetectors via carbon nanohorns and DMSO treatment," J. Mater. Chem. C **10**(35), 12809–12820 (2022).
68. P. Wan, M. Jiang, T. Xu, *et al.*, "High-mobility induced high-performance self-powered ultraviolet photodetector based on single ZnO microwire/PEDOT:PSS heterojunction via slight Ga-doping," J. Mater. Sci. Technol. **93**, 33–40 (2021).
69. X. Mo, X. Li, G. Dai, *et al.*, "All-inorganic perovskite $CsPbBr_3$ microstructures growth via chemical vapor deposition for high-performance photodetectors," Nanoscale **11**(44), 21386–21393 (2019).